ACS OMEGA

Open Access

This article is licensed under CC-BY 4.0

http://pubs.acs.org/journal/acsodf

Article

Fast and Facile Synthesis of Cobalt-Doped ZIF-8 and Fe_3O_4/MCC/Cobalt-Doped ZIF-8 for the Photodegradation of Organic Dyes under Visible Light

Amin Mehrehjedy, Piyush Kumar, Zachary Ahmad, Penelope Jankoski, Anuraj S. Kshirsagar, Jason D. Azoulay, Xuyang He, Mahesh K. Gangishetty, Tristan D. Clemons, Xiaodan Gu, Wujian Miao, and Song Guo*

Cite This: *ACS Omega* 2024, 9, 49239−49248

Read Online

ACCESS | Metrics & More | Article Recommendations | Supporting Information

ABSTRACT: Co-doped ZIF-8 as a water-stable visible light photocatalyst was prepared by using a one-pot, fast, cost-effective, and environmentally friendly method. The band structure of ZIF-8 was tuned through the incorporation of different percentages of cobalt to attain an optimal band gap (E_g) that enables the activation of ZIF-8 under visible light and minimizes the recombination of photogenerated charge carriers. A magnetic composite of Co-doped ZIF-8 was also synthesized to facilitate catalyst recycling and reusability through the application of an external magnetic field. Surface modification of magnetic Fe_3O_4 nanoparticles with microcrystalline cellulose (MCC) was used to reduce the level of agglomeration. The photocatalytic activities of Co-doped ZIF-8 (Co-ZIF-8) and Fe_3O_4/MCC/Co-ZIF-8 were evaluated for the photodegradation of methylene blue (MB) under visible light irradiation from a 20 W LED source. Co-ZIF-8 showed considerably higher photocatalytic activity than pure ZIF-8, confirming the success of the doping strategy. Both Co20%-ZIF-8 and Fe_3O_4/MCC/Co20%-ZIF-8 exhibited similar and remarkable photocatalytic activity under visible light (achieving 97% MB removal). The mechanism of photodegradation of MB by Fe_3O_4/MCC/Co20%-ZIF-8 was studied, revealing a first-order degradation kinetics (k = 13.78 × 10^{-3} min^{-1}), with peroxide and hole species as the predominant active reagents. The magnetic composite successfully displayed recyclability and reusability over multiple cycles with negligible reduction in MB photodegradation efficiency.

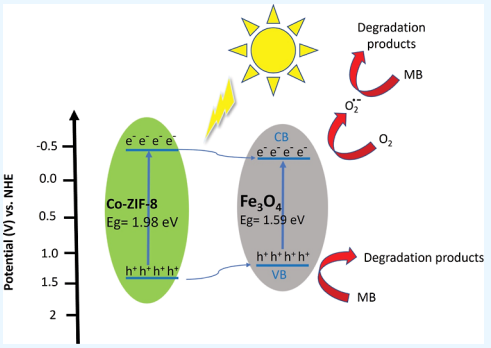

1. INTRODUCTION

Organic dyes are major contributors to water pollution in industrial wastewater. They are often toxic and difficult to decompose.[1] A green and energy-efficient method for their oxidative degradation is through photocatalytic degradation, which harnesses the power of UV and/or visible light in conjunction with a photocatalyst to generate reactive oxygen species (ROS).[2] While large band gap semiconductors are active in UV light, whose spectrum accounts for only a small fraction (3−5%) of sunlight.[3] On the other hand, although photocatalysts with small band gaps are effective under visible light, they often suffer from rapid recombination of photogenerated electron−hole pairs, hindering efficient electron transfer to other species in the aqueous medium and ROS production. Therefore, tuning the band gap and minimizing the charge recombination in the photocatalyst are necessary for efficient visible light activation.[2]

Metal−organic frameworks (MOFs) are a type of inorganic polymer developed recently. They consist of metal cluster centers and organic linkers, which enable various photo-induced charge transfer processes such as metal-to-ligand, ligand-to-metal, and ligand-to-ligand transfers.[4] MOFs have been utilized in various photocatalytic processes, including selective photooxidation of alcohols,[5] amine and sulfides,[4] water splitting,[6] photoreduction of CO_2,[7] and photocatalytic degradation of organic dyes.[8] MOFs stand out due to their high surface area, tunable cavity, and tailorable chemistry, which contribute to their superior activity compared to other alternatives.[9] Among the MOFs, zeolitic imidazolate frameworks (ZIFs) form a distinct subclass. ZIFs feature tetrahedrally coordinated transition metal ions connected by imidazolate ligands.[10] In the case of ZIF-8 and ZIF-67, the respective Zn^{2+} and Co^{2+} metal centers are linked by 2-methylimidazole (Hmim) to form a structure with a SOD (sodalite) topology.[11] While many MOFs, including ZIF-67,

Received: July 2, 2024
Revised: November 27, 2024
Accepted: November 29, 2024
Published: December 7, 2024

© 2024 The Authors. Published by American Chemical Society

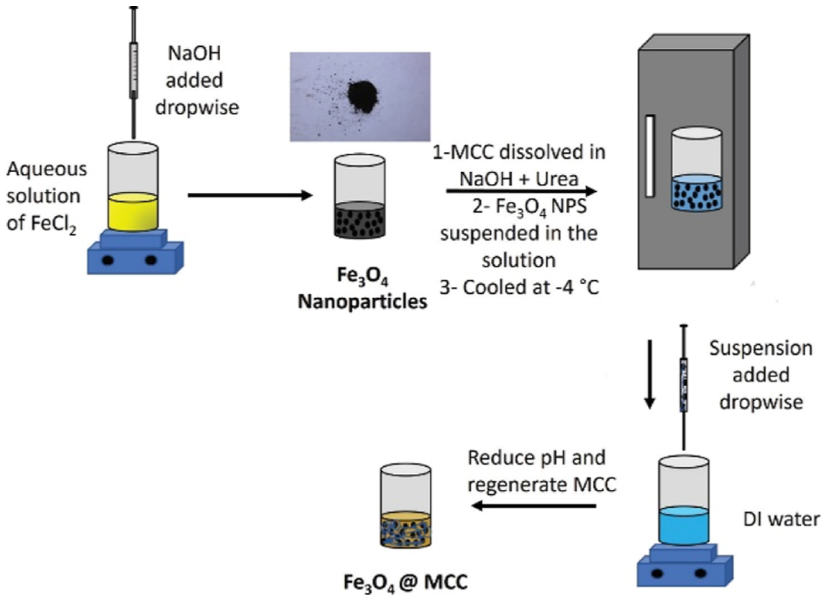

Figure 1. Synthesis of Fe_3O_4 and Fe_3O_4/ MCC.

are unstable in aqueous solutions, ZIF-8 exhibits water stability. However, its wide band gap (E_g = 5.1 eV) restricts its activity to UV light.[12] A recent report highlights the development of water-stable mixed metal derivatives of ZIF-8 and ZIF-67 with notable photocatalytic activity under visible light.[13]

Another challenge in the photocatalytic degradation of dyes in wastewater is the recycling and reuse of the photocatalyst. Coupling magnetic nanoparticles like iron oxides with the photocatalyst and separating them using a magnet presents a more favorable option compared to time- and energy-consuming processes such as filtration and centrifugation.[14] Magnetic nanoparticles have low photocatalytic activity due to their small band gap. To address this issue, modification of magnetic nanoparticles with materials possessing a finely tuned band gap, such as metal oxides[15−17] or MOFs,[18−20] has been explored to enhance their photocatalytic efficiency, resulting in the development of effective magnetic photocatalysts.[21] Previously reported methods for fabricating magnetic composites of MOFs, such as the solvothermal method, are time-consuming, taking several hours or even days to complete. These methods require significant amounts of energy, specialized equipment, and the use of organic solvents that are not environmentally friendly.[22,23] Therefore, a faster, less energy-consuming, low-cost, and environmentally friendly method for the fabrication of magnetic MOFs is necessary for their large-scale production.

Sunlight is available only during the daytime, and its supply can be interrupted by cloudy days or nighttime. To address this challenge, artificial light sources such as sunlight simulators, xenon arc lamps,[13] mercury-vapor lamp,[10] and LEDs[2] have been used as the light sources. Among these options, LEDs are the best alternative to sunlight due to their energy efficiency, durability, long lifespan, and ability to operate on direct current.[24]

In this study, we present a rapid and straightforward method for fabricating Co-ZIF-8s and their magnetic composites in alkaline aqueous solution. The synthesis can be completed in just 20 min and does not require any specialized equipment or heating. The photocatalytic activity of the prepared samples is evaluated through the photodegradation of methylene blue (MB) under visible light. Additionally, the mechanism of photodegradation is investigated by using scavenger tests and Mott−Schottky plots.

2. EXPERIMENTAL SECTION

2.1. Synthesis of ZIF-8, ZIF-67, and Co-Doped ZIF-8 and Their Magnetic Composite. All chemicals used were of analytical grade and were used without further purification. ZIF-8, ZIF-67, and mixed metal derivatives were synthesized using stoichiometric concentrated aqueous solutions of metal and ligand in the presence of ammonium hydroxide.[25−27] Zinc nitrate hexahydrate ($Zn(NO_3)_2{\cdot}6H_2O$) and cobalt(II) acetate ($Co(OOCCH_3)_2{\cdot}4H_2O$) were dissolved in deionized (DI) water at various ratios to prepare solution A. Additionally, 2-methylimidazole was dissolved in ammonium hydroxide (29% aqueous solution) to prepare solution B. Subsequently, solution B was added dropwise to solution A with a metal-to-ligand ratio of 1:2 under vigorous stirring. The resulting solution was continuously stirred for an additional 20 min to complete the crystallization of the ZIF samples. The precipitations were washed several times to reduce the pH and then dried in an oven at 80 °C overnight.

Fe_3O_4 magnetic nanoparticles were synthesized using a promising method for large-scale production, involving the partial oxidation of Fe^{2+} in an alkali solution. This method is simple, fast, and high yield.[28,29] As shown in Figure 1, NaOH was added to an aqueous solution of $FeCl^{2+}$ under vigorous stirring to obtain a black magnetic precipitate. The precipitate was then collected using an external magnet, washed multiple times with DI water to reduce the pH, and subsequently dried overnight in an oven to obtain Fe_3O_4 nanoparticles.

During composite synthesis, Fe_3O_4 magnetic nanoparticles tend to agglomerate, resulting in the formation of two solid phases instead of a uniform composite.[30] To tackle this issue, microcrystalline cellulose (MCC), a sustainable material, was used to modify the surface of magnetic nanoparticles and reduce agglomeration.[30,31] Fe_3O_4/MCC nanoparticles were prepared by dissolving cellulose in an aqueous solution of urea and NaOH at 0 °C. Subsequently, the magnetic nanoparticles

https://doi.org/10.1021/acsomega.4c06142
ACS Omega 2024, 9, 49239−49248

were dispersed in the solution, and MCC crystals were regenerated upon the pH reduction achieved by adding DI water.[32]

In the final step, magnetic composites of ZIFs were synthesized by dispersing Fe_3O_4/MCC in an aqueous solution of cobalt and zinc salt (Figure 2). Solution B was subsequently

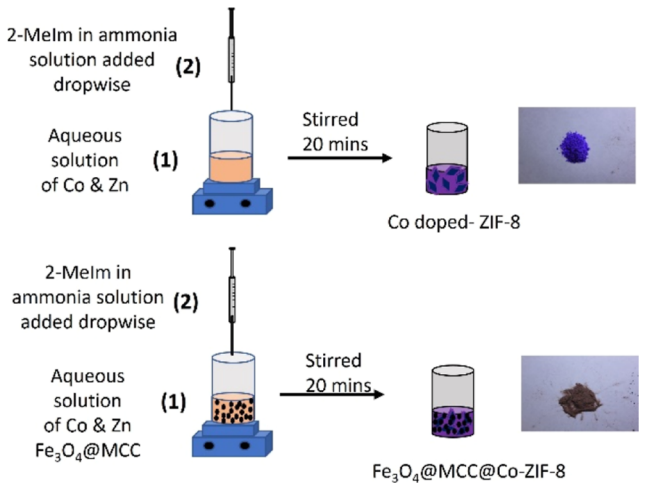

Figure 2. Synthesis of Co-ZIF-8 and Fe_3O_4/MCC/Co-ZIF-8.

added dropwise to the mixture under vigorous stirring, and the solution was stirred for an extra 20 min to complete the crystallization process. The resulting composite was washed several times with DI water to reduce the pH and then dried in an oven overnight.

2.2. Characterization. Powder wide-angle X-ray scattering (WAXS) data of the as-prepared samples were collected using a Xenocs Xeuss X-ray scattering beamline with Cu K-alpha (wavelength 0.15418 nm) radiation. The morphology of samples was observed by environmental scanning electron microscopy (ESEM, FEI Quanta) and transmission electron microscopy (TEM, Zeiss EM 900). SEM/EDX (ESEM, FEI Quanta with Thermo System 7 EDS X-ray detectors) was used to study the elemental composition of the samples. Fourier transform infrared spectroscopy (FT-IR) spectra were measured by a Nicolet Summit spectrometer. The ζ-potential was measured using a Zetasizer Nano ZSP instrument (Malvern). Diffuse reflectance spectroscopy (DRS) was performed using a Shimadzu UV-2600i spectrophotometer.

Electrochemical impedance spectroscopy studies were carried out by using an electrochemical analyzer (CH Instruments, CHI660A) in a standard three-electrode system. Slurries were prepared by dispersing the photocatalysts into a solution of H_2O, ethanol, and Nafion in the ratio of 75:20:5, with Nafion acting as a binder. The working electrode was fabricated by drop-casting 35 μL of slurry onto a carbon-cloth (CC) substrate electrode with a working area of (1 × 0.5) cm^2. The resulting electrode was then immersed in a 0.5 M Na_2SO_4 electrolyte. A saturated Ag/AgCl electrode and platinum mesh were used as the reference and counter electrodes, respectively. Mott−Schottky curves were plotted with the independence-potential model to estimate the band positions of Co-ZIF-8 and the magnetic composite.

2.3. Photocatalytic Experiment. The photocatalytic activities of different catalysts were investigated by degrading a model organic dye, MB, in solution under visible light. A water-jacketed photoreactor was equipped with a 20 W white LED lamp as the visible light source. A beaker containing 50 mL of MB solution and 50 mg of the catalyst was placed 20 cm away from the light source during the photodegradation process.

To achieve an adsorption−desorption equilibrium, the catalyst-MB suspension was stirred in the dark for 30 min prior to irradiation. Experiments were carried out at a constant temperature of 25 °C, and samples were collected every 30 min. Changes in the MB concentrations were measured by using a Cary 60 UV−visible spectrometer. The degradation of MB was monitored by analyzing the changes in the absorption spectrum at 665 nm.

3. RESULTS AND DISCUSSION

3.1. Catalyst Characterization. The WAXS data of the as-prepared ZIF samples, including ZIF-8 and ZIF-67, as shown in Figure 3, are consistent with previous reports.[13] The

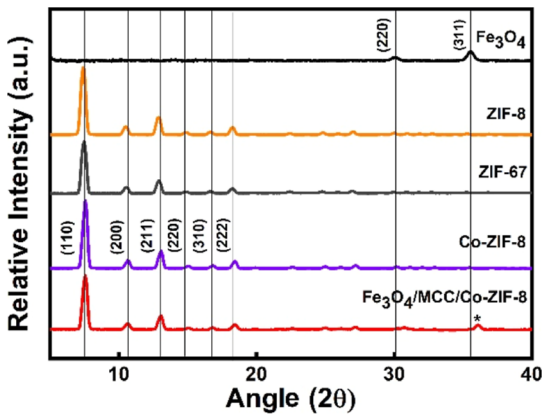

Figure 3. WAXS of ZIF-8, ZIF-67 (intensity × 2), Co-doped ZIF-8, Fe_3O_4, and Fe_3O_4/MCC/Co20%-ZIF-8 (intensity × 5). * denotes 2θ = 36° arising from the (311) of the magnetic Fe_3O_4 nanoparticles.

prominent peaks observed at 7.4, 10.6, 12.9, 14.9, 16.6, and 18.3° correspond to the (110), (200), (211), (220), (310), and (222) crystallographic planes, respectively. Both ZIF-8 and ZIF-67 exhibit peaks with identical 2θ values, confirming that they are in the same phase. In the cases of Co-ZIF-8 and Fe_3O_4/MCC/Co-ZIF-8, the same peaks are observed, confirming the existence of ZIF phases in the composite material. The ZIF peaks in the composite slightly shift to higher 2θ values (0.1°), which could be attributed to the doping effect from cobalt. In the WAXS of Fe_3O_4/MCC/Co-ZIF-8, the relative intensities of peaks are lower than those of the pure ZIF samples due to the presence of magnetic nanoparticles. However, the main peaks of Co-ZIF-8 are present in the spectra. The relative intensity of Fe_3O_4 peaks is lower than that of Co-ZIF-8, with only the main peak of magnetic nanoparticles (311) observed at 2θ = 36° as marked in the spectra.[33] The preserved ZIF and Fe_3O_4 peaks, as well as the absence of additional peaks, confirm the structural integrity of the synthesized composites.

In Figure 4, the FT-IR spectra of Fe_3O_4 exhibited a peak at 580 cm^{-1}, which is characteristic of Fe_3O_4 and corresponds to the Fe−O vibration. The FT-IR spectra of Fe_3O_4/MCC showed peaks at 1047, 1377, 1434, 1648, 2941, and 3426 cm^{-1}, attributed to C−O stretching, C−H and O−H bending, and C−H and O−H stretching of cellulose, respectively. All Co-doped ZIF materials, including Co-ZIF-8 and Fe_3O_4/

https://doi.org/10.1021/acsomega.4c06142
ACS Omega 2024, 9, 49239−49248

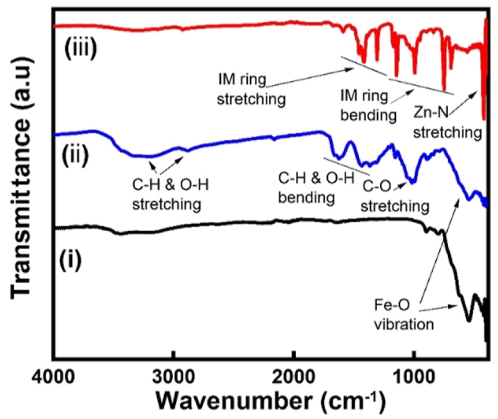

Figure 4. FT-IR of the as-prepared samples. (i) Fe_3O_4, (ii) Fe_3O_4/MCC, and (iii) Fe_3O_4/MCC/Co-ZIF-8.

MCC/Co-ZIF-8, show characteristic IR peaks of pure ZIF-8 and ZIF-67, as seen in Figure 4. In the case of Co-doped ZIF-8, the band at 421 cm^{-1} can be assigned to the Zn−N stretch mode, and the bands at 500−1350 cm^{-1} are attributed to plane bending. Peaks at 1350−1500 cm^{-1} are attributed to the plane stretching of the imidazole ring. Additionally, a C═N stretch mode was observed at 1584 cm^{-1}.[34,35] The FT-IR data indicate a successful integration between the ZIF, Fe_3O_4, and MCC phases within the composite materials.

The morphologies of the ZIFs and their composites were studied by SEM. The SEM image of Co-ZIF-8 shown in Figure 5A reveals larger plate-like particles compared to the smaller cube-like morphology typically observed for ZIF-8, ZIF-67, and their mixed-metal derivatives reported previously.[13] The observed morphology could be attributed to the vigorous stirring method used during synthesis,[36] which is necessary for the formation of a homogeneous magnetic composite of mixed metal ZIF-8. In Figure 5E, the Fe_3O_4 nanoparticles can be seen between the plate-like structures of Co-ZIF-8. Figure S2B shows a TEM image of a nanoparticle of Fe_3O_4. The TEM image of Co-ZIF-8 (Figure S2A) has a lighter contrast, likely due to the lower mass thickness of ZIF material compared to Fe_3O_4. The TEM image of Co-ZIF-8 also shows elongated structures that are consistent with the plate-like structure observed in SEM. For Fe_3O_4/MCC/Co-ZIF-8, both Fe_3O_4 and Co-ZIF-8 regions are present to form heterojunctions, as shown in Figure S2D.

The SEM/EDX mapping shows an even distribution of both Co and Zn in Co-ZIF-8, indicating successful doping with ZIF-8 (Figure 5C,D). EDX mapping of Fe_3O_4/MCC/Co-ZIF-8 (Figure 5G−I) demonstrates a uniform distribution of Co, Zn, and Fe, confirming that Co-ZIF-8 are evenly grown on Fe_3O_4/MCC, providing ample interfaces between them. Therefore, it is very likely that a heterojunction is formed between Fe_3O_4 and Co-ZIF-8, consistent with SEM, WAXS, and FTIR results.

Figure 6 shows the magnetic hysteresis curve of Fe_3O_4 and Fe_3O_4/MCC/Co-doped ZIF-8 nanocomposites at 2, 10, and 300 K to study their magnetic behaviors under varying temperatures. The saturation magnetization is notably higher at 2 and 10 K compared to 300 K due to reduced thermal agitation at lower temperatures. The hysteresis loops of the Fe_3O_4 and Fe_3O_4/MCC/Co-doped ZIF-8 nanoparticles exhibit ferromagnetic behavior. The magnetization saturation of Fe_3O_4/MCC/Co-doped ZIF-8 is smaller than that of Fe_3O_4 nanoparticles due to the addition of nonmagnetic Co-doped

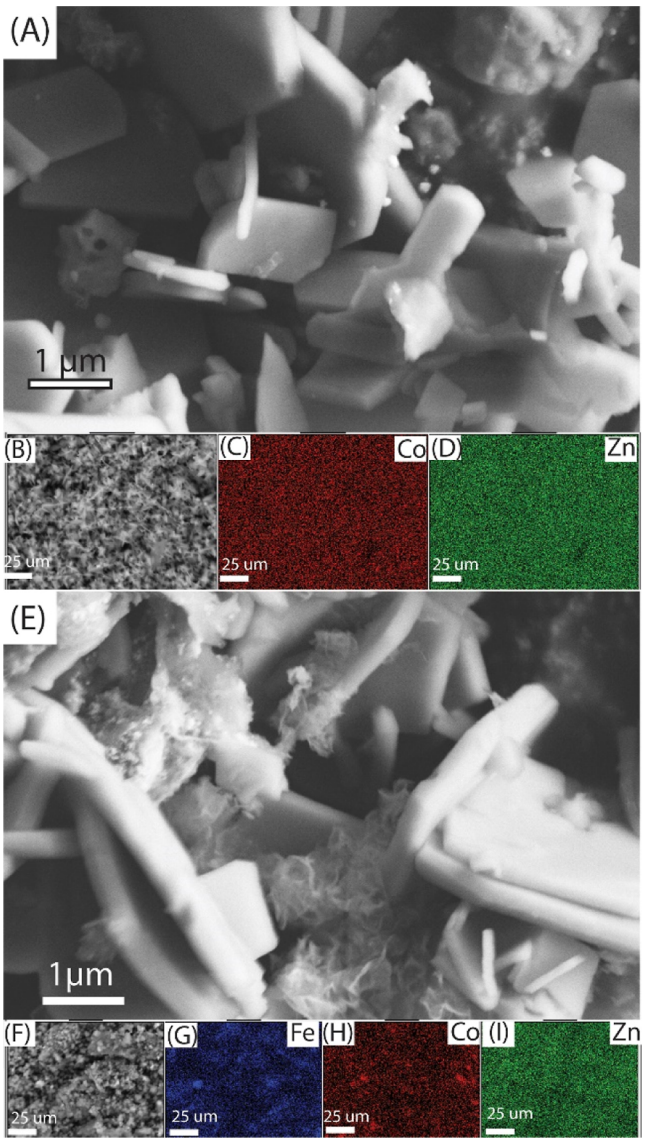

Figure 5. Representative scanning electron micrographs of (A,B) Co-ZIF-8 and (E,F) Fe_3O_4/MCC/Co-ZIF-8 and the corresponding elemental mapping of (C,D) Co-ZIF-8 and (G−I) Fe_3O_4/MCC/Co-ZIF-8.

ZIF-8 and MCC, which decreases the total magnetic moment in the sample. Additionally, as shown in Figure 6C,D, both Fe_3O_4 and Fe_3O_4/MCC/Co-ZIF-8 are magnetic and are attracted to an external magnet.

DLS analysis was used to measure the zeta potential and size distribution of the magnetic samples. The zeta potential measurements displayed in Figure 7A confirm an increase in the magnitude of the negative zeta potential, indicating a strengthening of repulsive forces between particles, thereby reducing agglomeration. This validates the successful implementation of cellulose as a strategy to mitigate agglomeration. Furthermore, the functionalization of Fe_3O_4/MCC with Co-ZIF-8 does not result in a significant reduction of the zeta potential to lower values but maintains negative zeta potentials. These negative zeta potentials contribute to better dispersion of the photocatalyst in the photocatalytic reaction media via electrostatic repulsions. Figure 7B shows the plots of size distribution of Fe_3O_4 to Fe_3O_4/MCC and Fe_3O_4/MCC/Co-ZIF-8, with peaks around 160, 300, and 630 nm, respectively.

https://doi.org/10.1021/acsomega.4c06142
ACS Omega 2024, 9, 49239−49248

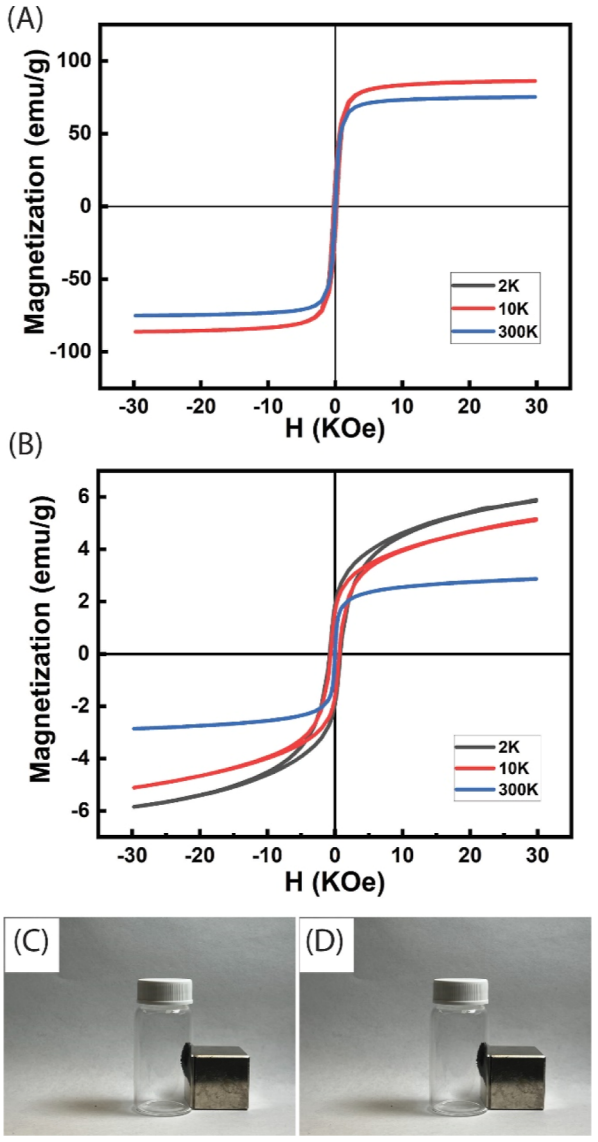

Figure 6. Magnetic hysteresis curve of (A) Fe_3O_4 and (B) Fe_3O_4/MCC/Co-ZIF-8. Photographs of the magnetic separation of (C) Fe_3O_4 and (D) Fe_3O_4/MCC/Co-ZIF-8 with a permanent magnet (photograph courtesy of A.M., Copyright 2024).

This confirms that particle sizes increase when Fe_3O_4 is modified with MCC and increase further after modification with Co-ZIF-8. The broader peaks of Fe_3O_4/MCC and Fe_3O_4/MCC/Co-ZIF-8 compared to that of Fe_3O_4 indicate a wider range of particle sizes for these composite materials.

3.2. Photocatalytic Degradation of MB by Different Catalysts. The photodegradation of MB by a catalyst under visible light irradiation was examined, revealing the enhanced performance of Co-ZIF-8s compared with that of ZIF-8. The Co-ZIF-8 samples demonstrated superior activity, achieving a degradation rate of 91% within a 3 h time frame, whereas ZIF-8 achieved around 65% degradation within the same period, as shown in Figure 8A. This outcome verifies the success of our doping strategy in enhancing the photocatalytic activity of ZIF-8 under visible light. Among the Co-ZIF-8 samples, their photodegradation activities were generally comparable, with Co20%-ZIF-8 exhibiting slightly better results. Notably, Co20%-ZIF-8 displayed degradation rates of 75%, 91%, and 97.5% for MB within 120, 150, and 180 min, respectively.

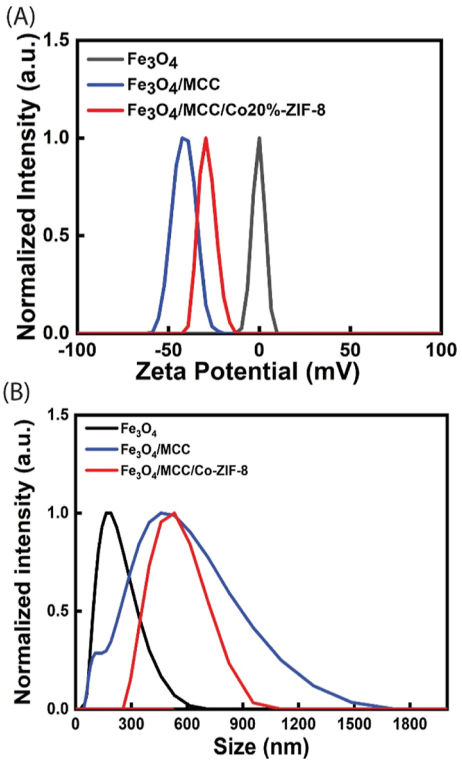

Figure 7. (A) ζ-Potential of Fe_3O_4, Fe_3O_4/MCC, and Fe_3O_4/MCC/Co-ZIF-8. (B) Size distribution of Fe_3O_4, Fe_3O_4/MCC, and Fe_3O_4/MCC/Co-ZIF-8.

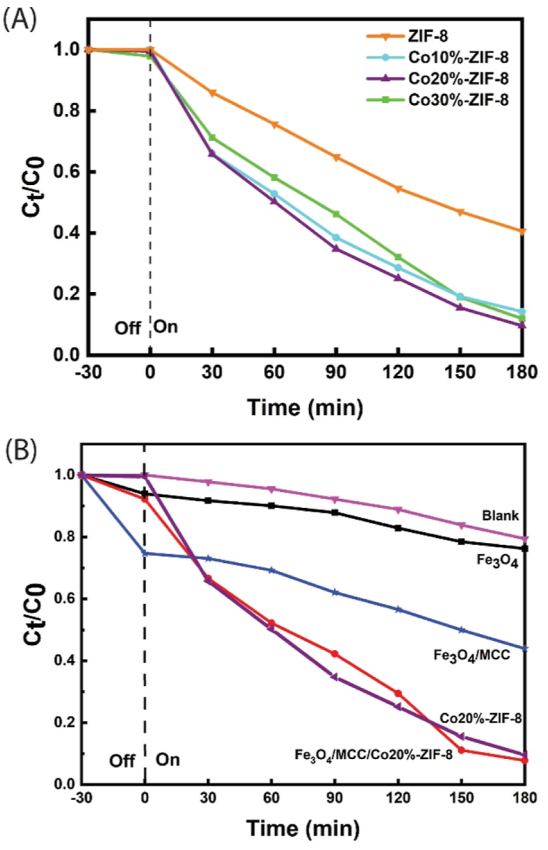

Figure 8. Photodegradation of MB under visible light irradiation by (a) different ZIF samples. (b) Different magnetic composites vs Co20%-ZIF-8.

https://doi.org/10.1021/acsomega.4c06142
ACS Omega 2024, 9, 49239−49248

Consequently, the Co20%-ZIF-8 sample was chosen for the fabrication of the magnetic composite of Co-ZIF-8 (Figure 1). A control experiment was carried out to assess the self-sensitized photodegradation of MB without utilizing any catalyst (blank in Figure 8B), showing that the MB degradation under the same 20 W lamp irradiation over a 3 h period was negligible.

Fe_3O_4 exhibited low photodegradation activity due to its small band gap and rapid recombination of photogenerated charge carriers, consistent with reports from previous studies.[37] The Fe_3O_4/MCC composite demonstrated notably higher MB removal in the dark compared to other samples. This outcome indicates that the primary mechanism behind MB removal by Fe_3O_4/MCC is adsorption, rather than photodegradation. The results of the zeta potential measurements showed that the surface of Fe_3O_4/MCC is negatively charged, facilitating the electrostatic interactions with the positively charged MB.[38] Initially, there is rapid adsorption of MB by Fe_3O_4/MCC, but the rate of MB removal diminishes gradually as the adsorption sites on the surface of Fe_3O_4/MCC become saturated.

As previously mentioned, the photodegradation of MB by Co-doped ZIFs is superior to that of ZIF-8. Figure 8B demonstrates that the Fe_3O_4/MCC/Co20%-ZIF-8 composite also exhibits excellent photocatalytic activity, with MB photodegradation rates of 71%, 93%, and 97% within 90, 120, and 180 min, respectively. These findings confirm that the photocatalytic activity of Fe_3O_4/MCC/Co20%-ZIF-8 surpasses that of Fe_3O_4 and Fe_3O_4/MCC magnetic composite and is comparable to that of Co20%-ZIF8, indicating that Co20%-ZIF-8 retain its catalytic performance on the surface of the Fe_3O_4/MCC magnetic composite. This outcome is consistent with our characterization data, which show the preservation of ZIF crystallinity in the composite materials and demonstrate the success of our approach in enhancing the photocatalytic activity of Fe_3O_4 nanoparticles through the incorporation of Co20%-ZIF-8.

3.3. Radical Scavenger and Reusability Test. Electron (e), hole (h^+), superoxide radicals ($O_2^{\bullet-}$), and hydroxyl radicals ($^\bullet$OH) are typical reactive species in the photocatalytic process. To investigate the photodegradation mechanism of MB by Fe_3O_4/MCC/Co20%-ZIF-8, radical scavengers were employed to trap potential photogenerated ROS. $AgNO_3$, CH_3OH, acrylamide, and *t*-butyl alcohol were used to scavenge the electron, hole, superoxide radicals, and hydroxyl radicals, respectively. As shown in Figure 9A, a significant decrease in the MB photodegradation was observed upon the application of hole and superoxide scavengers, suggesting that hole and superoxide radicals are the major ROS involved in the degradation of MB by the catalyst. Moreover, the reusability of the magnetic composite catalyst was tested by comparing the photocatalytic degradation of MB by Fe_3O_4/MCC/Co20%-ZIF-8 after six consecutive runs. The catalyst was recaptured from the reaction mixture readily using a magnet and washed before the next run. As shown in Figure 9B, the minimal decrease in photocatalytic degradation over six runs demonstrates the magnetic catalyst's excellent reusability. The XRD (Figure S3) and SEM (Figure S4) of the recycled Fe_3O_4/MCC/Co20%-ZIF-8 composite confirmed that it retains the morphology and crystalline structure after 6 runs.

3.4. Band Structure of the Photocatalysts. The optical properties of Fe_3O_4, ZIF-8, ZIF-67, and Co20%-ZIF-8 were studied using DRS, and the results are shown in Figure 10A. The DRS data were used to generate Tauc plots to estimate

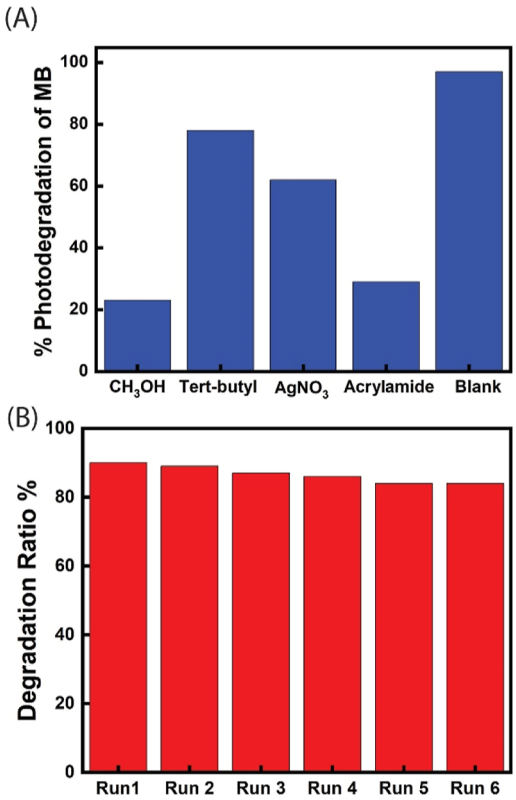

Figure 9. (A) Effects of different radical scavengers on the photodegradation of MB. (B) Photodegradation ratio of the catalyst at 180 min in six consecutive cycles.

the band gaps of the mentioned samples. This analysis was performed to assess the effect of cobalt doping on the band gap of ZIF-8. Additionally, the band gap values along with the estimated valence band (VB) and conduction band positions were used to determine the band alignment between Fe_3O_4 and Co20%-ZIF-8, which is critical for explaining the mechanism of electron transfer within the composite. The band gaps were determined by plotting $(\alpha h\nu)^2$ and $(\alpha h\nu)^{1/2}$ for direct and indirect band gaps vs photon energies, followed by extrapolating the linear regions to the energy axis, as shown in Figure 10B,C, respectively.[39−41] The calculated band gaps for ZIF-8, ZIF-67, and Co-ZIF-8 are 5.15, 1.89, and 1.98 eV, respectively. The results confirm that cobalt doping successfully decreases the band gap of ZIF-8, which could explain the enhanced photocatalytic activity of Co-ZIF-8 under visible light. The band gap of Fe_3O_4 was also calculated as 1.59 eV.

Mott−Schottky plots were used to determine the flat bands and, consequently, the conduction bands (CB) of Fe_3O_4 and Co20%-ZIF-8. By knowing the band gap from DRS analysis, the VB of these materials can be calculated. So, the data from DRS and Mott−Schottky plots allow us to understand the energy levels and charge transport behavior in the investigated Fe_3O_4/MCC/Co20%-ZIF-8 composite. As shown in Figure 11, the positive slope of Mott−Schottky plots indicates that both Fe_3O_4 and Co20%-ZIF-8 are n-type semiconductors.[42] The flat bands of both samples were estimated as −0.43 and −0.48 V versus Ag/AgCl (saturated KCl) and −0.23 and −0.28 V versus SHE, respectively.

According to the literature,[43] the CB of n-type semiconductors are more negative by about 0.1 V than their flat potentials. Therefore, the CB of Fe_3O_4 and Co20%-ZIF-8 were

https://doi.org/10.1021/acsomega.4c06142
ACS Omega 2024, 9, 49239−49248

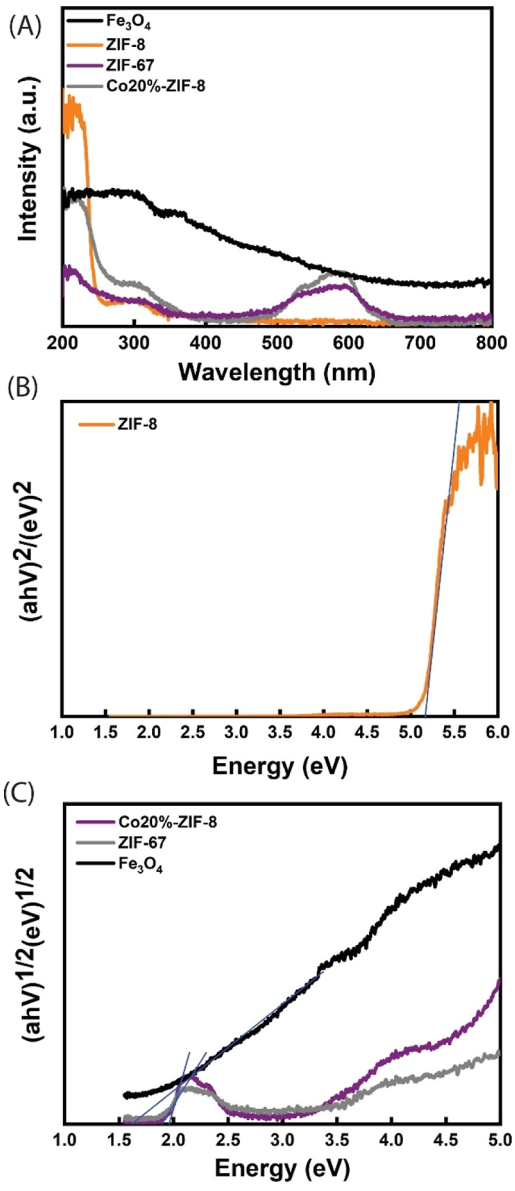

Figure 10. (A) UV−vis diffuse reflectance spectra of Fe_3O_4, ZIF-8, ZIF-67, and Co20%-ZIF-8. Tauc plots: (B) ZIF-8, (C) Fe_3O_4, ZIF-67, and Co20%-ZIF-8.

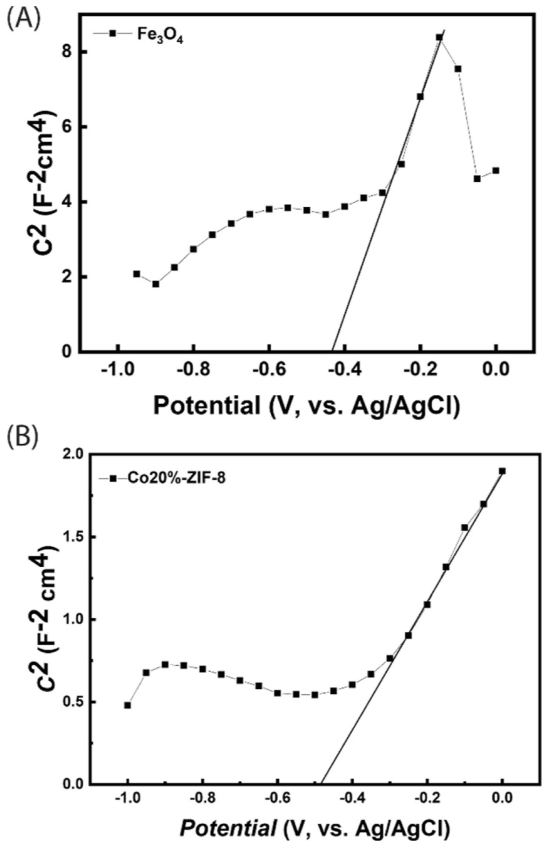

Figure 11. Mott−Schottky plots for (A) Fe_3O_4 and (B) Co20%-ZIF-8 electrodes.

estimated to be −0.33 and −0.38 V vs SHE, respectively. Given the band gaps of Fe_3O_4 (1.59 eV) and Co20%-ZIF-8 (1.98 eV), the corresponding VB potentials are 1.26 and 1.6 V vs SHE. The values of CB potentials are close to the redox potential of the $O_2/O_2^{\bullet-}$ couple (−0.33 V vs SHE), suggesting that the photocatalysts can transfer electrons to oxygen to produce the superoxide. This finding is consistent with the results of scavenger's tests used to study the mechanism of photodegradation of MB, which showed that holes and superoxide radicals are the major ROS involved in the degradation process.

3.5. Rate Order of the Photocatalytic Degradation of MB by As-Prepared Samples. The kinetics of the photodegradation of MB using Fe_3O_4/MCC/Co20%-ZIF-8 as the photocatalyst were studied. By examining both pseudo-first- and pseudo-second-order kinetics, the order of the reaction was determined. For pseudo-first-order kinetics, ln (C_0/C_t) was plotted against time, while for pseudo-second-order kinetics, $(1/C_t - 1/C_0)$ was plotted against time. The obtained linear fitting correlation constants were 0.97 and 0.77 for Co20%-ZIF-8 in the pseudo-first-order and pseudo-second-order kinetics, respectively. Similarly, for Fe_3O_4/MCC/Co20%-ZIF-8, the correlation constants were found to be 0.92 and 0.68 for the pseudo-first-order and pseudo-second-order kinetics, respectively. These results indicate that the photocatalytic degradation kinetics of Fe_3O_4/MCC/Co20%-ZIF-8 follows a pseudo-first-order reaction.

The photodegradation rate constants for Co20%-ZIF-8 and Fe_3O_4/MCC/Co20%-ZIF-8 are 12.61×10^{-3} and 13.78×10^{-3} min^{-1}, respectively. These findings demonstrate that the inclusion of the magnetic composite (Fe_3O_4/MCC) does not compromise the photocatalytic efficiency of the standalone Co-doped ZIF-8 (see Figure S1 in Supporting Information).

3.6. Photodegradation Mechanism. As mentioned earlier, the CB of Co-ZIF-8 is more negative than the redox potential of E^0 $(O_2/O_2^{\bullet-})$ = −0.33 eV vs SHE. This allows Co-ZIF-8 to produce the radical superoxide (eq 2). Additionally, the photogenerated holes can be directly transferred to the MB (eq 1). As discussed earlier, Co(II) reduces the band gap and activates the ZIF-8 under visible light, while also acting as an electron-trapping agent to quench the recombination of photogenerated electrons and holes in Co-ZIF-8.[44] The schematic of the proposed mechanism of Co20%-ZIF-8 is illustrated in Figure 12A.

Photocatalyst composites have different types of charge transfer based on their band alignment.[45,46] In the Fe_3O_4/MCC/Co20%-ZIF-8 composite the band edges of the Fe_3O_4 contain those of Co-ZIF-8, and the system forms a type I heterojunction. In this heterojunction, both photogenerated

https://doi.org/10.1021/acsomega.4c06142
ACS Omega 2024, 9, 49239−49248

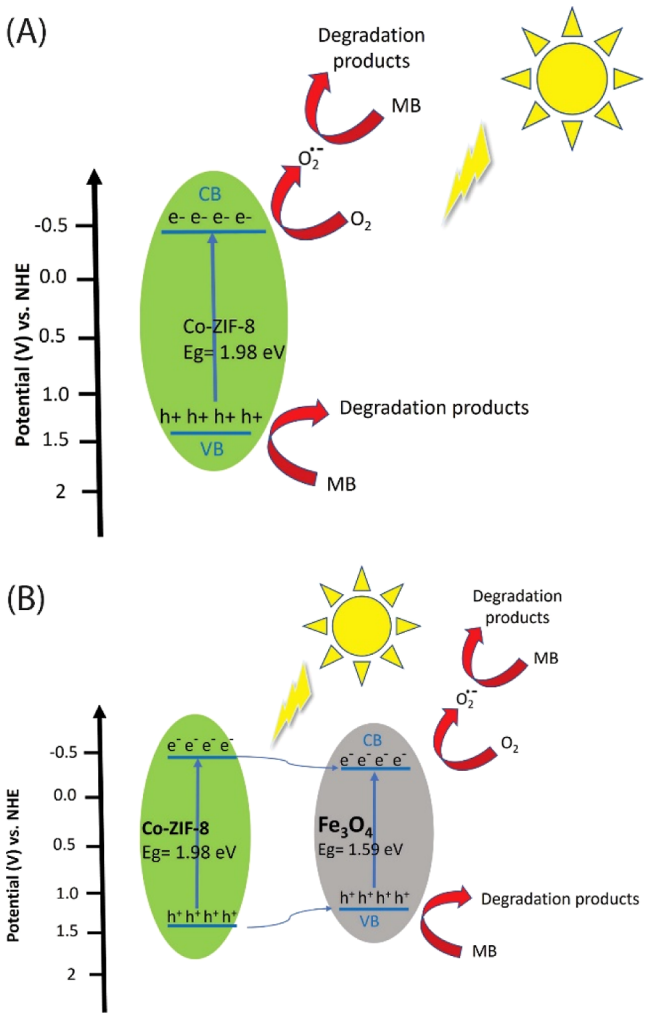

Figure 12. Schematic diagram of the proposed mechanism of photodegradation of MB by (A) Co-ZIF8 and (B) Fe_3O_4/MCC/Co20%-ZIF-8.

electrons and holes are concentrated on the CB and VB of Fe_3O_4, respectively. Although Type I heterojunctions suffer from reduction on redox potential,[47] this effect is not significant for the composite's performance in MB removal. This is because the CB of Fe_3O_4 is close to the CB of Co-ZIF-8, as well as the oxygen reduction potential. Additionally, holes can also be transferred to the MB from the VB of Fe_3O_4 (eq 1). The Type 1 heterojunction promotes electron−hole separation and inhibits the recombination of photogenerated electrons and holes in Fe_3O_4.

The concentrated electrons on the CB band of Fe_3O_4 have a high enough reduction potential and reduce oxygen to radical superoxide (E^0 ($O_2/O_2^{\bullet-}$) = −0.33 eV vs SHE), making superoxide the primary ROS for MB degradation.[48] (eq 2). The oxidation potential of the h_{VB}^+ is not strong enough to oxidize OH^- and produce $^{\bullet}OH$ radicals (E^0 ($OH^-/^{\bullet}OH$) = 1.99 eV vs SHE).[48] So, the degradation of MB by hydroxyl radicals is minor. According to scavenger experiments, direct oxidation of MB by holes is the second major degradation process after radical superoxide degradation (eqs 1 and 3). The schematic of the proposed mechanism of Fe_3O_4/MCC/Co20%-ZIF-8 is shown in Figure 12B.

$$h_{VB}^+ + MB \rightarrow MB^{\bullet+} \rightarrow \text{MB degradation products} \quad (1)$$

$$e_{VB}^- + O_2 \rightarrow O_2^{\bullet-} \quad (2)$$

$$MB + O_2^{\bullet-} \rightarrow \text{MB degradation products} \quad (3)$$

4. CONCLUSIONS

This study reports on a green, facile, fast, and low-cost method for synthesizing cobalt-doped ZIF-8s and their magnetic composites. The photocatalytic activity of the prepared composites was assessed by studying the photodegradation of MB under visible light irradiation using LEDs. The cobalt-doped ZIF-8 samples exhibited superior activity compared to ZIF-8 in the photodegradation of MB. The rate constants of photodegradation of MB by Co20%-ZIF-8 and Fe_3O_4/MCC/Co20%-ZIF-8 were found to be 12.61×10^{-3} min^{-1} and 13.78×10^{-3} min^{-1}, respectively. These results confirm that coupling Co20%-ZIF-8 to magnetic nanoparticles did not decrease the photocatalytic activity. Scavenger tests and Mott−Schottky plots were used to investigate the mechanism of the photodegradation. These experiments revealed that both Co20%-ZIF-8 and Fe_3O_4/MCC/Co20%-ZIF-8 produce holes and superoxide as major ROS upon visible light irradiation. Fe_3O_4/MCC/Co20%-ZIF-8 was easily separated from the aqueous media by a magnet and could be recycled and reused for three consecutive cycles without a significant decrease in its photocatalytic activity.

■ ASSOCIATED CONTENT

Supporting Information

The Supporting Information is available free of charge at https://pubs.acs.org/doi/10.1021/acsomega.4c06142.

Additional figures including kinetic model fittings for the photodegradation as discussed in the main text (PDF)

■ AUTHOR INFORMATION

Corresponding Author

Song Guo − *Department of Chemistry and Biochemistry, School of Mathematics and Natural Sciences, University of Southern Mississippi, Hattiesburg, Mississippi 39406, United States;* orcid.org/0000-0002-3457-4331; Phone: (+1) 601-266-4702; Email: song.guo/usm.edu

Authors

Amin Mehrehjedy − *Department of Chemistry and Biochemistry, School of Mathematics and Natural Sciences, University of Southern Mississippi, Hattiesburg, Mississippi 39406, United States*

Piyush Kumar − *Department of Chemistry and Biochemistry, School of Mathematics and Natural Sciences, University of Southern Mississippi, Hattiesburg, Mississippi 39406, United States*

Zachary Ahmad − *School of Polymer Science and Engineering, The University of Southern Mississippi, Hattiesburg, Mississippi 39406, United States*

Penelope Jankoski − *School of Polymer Science and Engineering, The University of Southern Mississippi, Hattiesburg, Mississippi 39406, United States*

Anuraj S. Kshirsagar − *Department of Chemistry, Mississippi State University, Starkville, Mississippi 39762, United States*

Jason D. Azoulay − *School of Chemistry and Biochemistry and School of Materials Science and Engineering, Georgia Institute of Technology, Atlanta, Georgia 30332, United States*

https://doi.org/10.1021/acsomega.4c06142
ACS Omega 2024, 9, 49239−49248

Xuyang He − *School of Criminal Justice, Forensic Science, and Security, The University of Southern Mississippi, Hattiesburg, Mississippi 39406, United States;* orcid.org/0000-0003-0435-4255

Mahesh K. Gangishetty − *Department of Chemistry, Mississippi State University, Starkville, Mississippi 39762, United States; Department of Physics and Astronomy, Mississippi State University, Mississippi State, Mississippi 39762, United States*

Tristan D. Clemons − *School of Polymer Science and Engineering, The University of Southern Mississippi, Hattiesburg, Mississippi 39406, United States;* orcid.org/0000-0001-8042-0141

Xiaodan Gu − *School of Polymer Science and Engineering, The University of Southern Mississippi, Hattiesburg, Mississippi 39406, United States;* orcid.org/0000-0002-1123-3673

Wujian Miao − *Department of Chemistry and Biochemistry, School of Mathematics and Natural Sciences, University of Southern Mississippi, Hattiesburg, Mississippi 39406, United States;* orcid.org/0000-0002-8008-7200

Complete contact information is available at: https://pubs.acs.org/10.1021/acsomega.4c06142

Author Contributions

The manuscript was written through contributions of all authors. All authors have given approval to the final version of the manuscript.

Notes

The authors declare no competing financial interest.

■ ACKNOWLEDGMENTS

This work was supported by the National Science Foundation under grant no. 1554841. The authors would like to thank Michael Blanton for his help in SEM measurements.

■ ABBREVIATIONS

MOF	metal−organic frameworks
ZIF	zeolite imidazolate frameworks
MB	methylene blue
ROS	reactive oxygenated species
SOD	sodalite
2-MeIm	2-methylimidazole
MCC	microcrystalline cellulose
FT-IR	Fourier-transform infrared spectroscopy
EIS	electrochemical impedance spectroscopy
WAXS	wide-angle X-ray spectroscopy
SEM	scanning electron microscopy
VB	valence band
CB	conduction band

■ REFERENCES

(1) Villanueva, C. M.; Kogevinas, M.; Cordier, S.; Templeton, M. R.; Vermeulen, R.; Nuckols, J. R.; Nieuwenhuijsen, M. J.; Levallois, P. Assessing Exposure and Health Consequences of Chemicals in Drinking Water: Current State of Knowledge and Research Needs. *Environ. Health Perspect.* **2014**, *122* (3), 213−221.

(2) Rahimi, R.; Mehrehjedy, A.; Zargari, S. $BiVO_4$ /Mn_3O_4 a Novel p-n Heterojunction Photocatalyst Functionalized with Metalloporphyrins: Synthesis, Charge Transfer Mechanism, and Enhanced Visible-Light Photocatalysis for Degradation of Dye Pollutant. *Environ. Prog. Sustain. Energy* **2017**, *36* (5), 1439−1448.

(3) Ajmal, A.; Majeed, I.; Malik, R. N.; Idriss, H.; Nadeem, M. A. Principles and Mechanisms of Photocatalytic Dye Degradation on TiO_2 Based Photocatalysts: A Comparative Overview. *RSC Adv.* **2014**, *4* (70), 37003−37026.

(4) Wei, H.; Guo, Z.; Liang, X.; Chen, P.; Liu, H.; Xing, H. Selective Photooxidation of Amines and Sulfides Triggered by a Superoxide Radical Using a Novel Visible-Light-Responsive Metal−Organic Framework. *ACS Appl. Mater. Interfaces* **2019**, *11* (3), 3016−3023.

(5) Wang, D.; Li, Z. Bi-Functional NH_2 -MIL-101(Fe) for One-Pot Tandem Photo-Oxidation/Knoevenagel Condensation between Aromatic Alcohols and Active Methylene Compounds. *Catal. Sci. Technol.* **2015**, *5* (3), 1623−1628.

(6) Wang, W.; Xu, X.; Zhou, W.; Shao, Z. Recent Progress in Metal-Organic Frameworks for Applications in Electrocatalytic and Photocatalytic Water Splitting. *Adv. Sci.* **2017**, *4* (4), 1600371.

(7) Li, R.; Zhang, W.; Zhou, K. Metal−Organic-Framework-Based Catalysts for Photoreduction of CO_2. *Adv. Mater.* **2018**, *30* (35), 1705512.

(8) Bedia, J.; Muelas-Ramos, V.; Peñas-Garzón, M.; Gómez-Avilés, A.; Rodríguez, J.; Belver, C. A Review on the Synthesis and Characterization of Metal Organic Frameworks for Photocatalytic Water Purification. *Catalysts* **2019**, *9* (1), 52.

(9) Wang, C.; Liu, D.; Lin, W. Metal−Organic Frameworks as A Tunable Platform for Designing Functional Molecular Materials. *J. Am. Chem. Soc.* **2013**, *135* (36), 13222−13234.

(10) Boruah, P. K.; Borthakur, P.; Das, M. R. Magnetic Metal/Metal Oxide Nanoparticles and Nanocomposite Materials for Water Purification. In *Nanoscale Materials in Water Purification*; Elsevier, 2019; pp 473−503.

(11) Tang, J.; Salunkhe, R. R.; Zhang, H.; Malgras, V.; Ahamad, T.; Alshehri, S. M.; Kobayashi, N.; Tominaka, S.; Ide, Y.; Kim, J. H.; Yamauchi, Y. Bimetallic Metal-Organic Frameworks for Controlled Catalytic Graphitization of Nanoporous Carbons. *Sci. Rep.* **2016**, *6* (1), 30295.

(12) Taheri, M.; Enge, T. G.; Tsuzuki, T. Water Stability of Cobalt Doped ZIF-8: A Quantitative Study Using Optical Analyses. *Mater. Today Chem.* **2020**, *16*, 100231.

(13) Saliba, D.; Ammar, M.; Rammal, M.; Al-Ghoul, M.; Hmadeh, M. Crystal Growth of ZIF-8, ZIF-67, and Their Mixed-Metal Derivatives. *J. Am. Chem. Soc.* **2018**, *140* (5), 1812−1823.

(14) Meteku, B. E.; Huang, J.; Zeng, J.; Subhan, F.; Feng, F.; Zhang, Y.; Qiu, Z.; Aslam, S.; Li, G.; Yan, Z. Magnetic Metal−Organic Framework Composites for Environmental Monitoring and Remediation. *Coord. Chem. Rev.* **2020**, *413*, 213261.

(15) Afkari, M.; Masoudpanah, S. M.; Hasheminiasari, M.; Alamolhoda, S. Effects of Iron Oxide Contents on Photocatalytic Performance of Nanocomposites Based on G-C_3N_4. *Sci. Rep.* **2023**, *13* (1), 6203.

(16) López, J.; Rey, A.; Viñuelas-Zahinos, E.; Álvarez, P. M. Preparation of a New Green Magnetic Fe_3O_4@TiO_2-P25 Photocatalyst for Solar Advanced Oxidation Processes in Water. *J. Environ. Chem. Eng.* **2023**, *11* (3), 109999.

(17) Anjana, P. M.; Joe Sherin, J. F.; Vijayakumar, C.; Sarath Kumar, S. R.; Bindhu, M. R.; Rakhi, R. B. Role of Reduced Graphene Oxide-Co-Double-Doped Fe3O4 Nanocomposites for Photocatalytic and Supercapacitor Applications. *Mater. Sci. Eng., B* **2023**, *290*, 116313.

(18) Yeganeh, M.; Farzadkia, M.; Jonidi Jafari, A.; Sobhi, H. R.; Esrafili, A.; Gholami, M. Utilization of the Copper Recovered from Waste Printed Circuit Boards as a Metal Precursor for the Synthesis of TiO_2/Magnetic-MOF(Cu) Nanocomposite: Application in Photocatalytic Degradation of Pesticides in Aquatic Solutions. *J. Environ. Manage.* **2023**, *345*, 118755.

(19) Yang, X.; Pan, J.; Hu, J.; Zhao, S.; Cheng, K. MOF-Derived La−$ZnFe_2O_4$@Fe_3O_4@carbon Magnetic Hybrid Composite as a Highly Efficient and Recyclable Photocatalyst for Mycotoxins Degradation. *Chem. Eng. J.* **2023**, *467*, 143381.

(20) Wang, K.; Huang, Z.; Jin, X.; Zhang, D.; Wang, J. MOF−Derived Hollow Porous $ZnFe_2O_4$/AgCl/Ag/C Nanotubes with Magnetic−Dielectric Synergy as High−Performance Photocatalysts for Hydrogen Evolution Reaction. *Chem. Eng. J.* **2021**, *422*, 130140.

(21) Shukla, S.; Khan, R.; Daverey, A. Synthesis and Characterization of Magnetic Nanoparticles, and Their Applications in Wastewater Treatment: A Review. *Environ. Technol. Innov.* **2021**, *24*, 101924.
(22) Zhao, G.; Qin, N.; Pan, A.; Wu, X.; Peng, C.; Ke, F.; Iqbal, M.; Ramachandraiah, K.; Zhu, J. Magnetic Nanoparticles@Metal-Organic Framework Composites as Sustainable Environment Adsorbents. *J. Nanomater.* **2019**, *2019*, 1−11.
(23) Gao, Y.; Liu, G.; Gao, M.; Huang, X.; Xu, D. Recent Advances and Applications of Magnetic Metal-Organic Frameworks in Adsorption and Enrichment Removal of Food and Environmental Pollutants. *Crit. Rev. Anal. Chem.* **2020**, *50* (5), 472−484.
(24) Jerlin Jose, Y.; Manjunathan, M.; Joseph Selvaraj, S. Highly Photocatalyst Efficient in LEDs/Solar Active and Reusable: Sm−ZnO−Ag Nanoparticles for Methylene Blue Degradation. *J. Nanostruct. Chem.* **2017**, *7* (3), 259−271.
(25) He, M.; Yao, J.; Liu, Q.; Wang, K.; Chen, F.; Wang, H. Facile Synthesis of Zeolitic Imidazolate Framework-8 from a Concentrated Aqueous Solution. *Microporous Mesoporous Mater.* **2014**, *184*, 55−60.
(26) Chen, B.; Bai, F.; Zhu, Y.; Xia, Y. A Cost-Effective Method for the Synthesis of Zeolitic Imidazolate Framework-8 Materials from Stoichiometric Precursors via Aqueous Ammonia Modulation at Room Temperature. *Microporous Mesoporous Mater.* **2014**, *193*, 7−14.
(27) Yao, J.; He, M.; Wang, K.; Chen, R.; Zhong, Z.; Wang, H. High-Yield Synthesis of Zeolitic Imidazolate Frameworks from Stoichiometric Metal and Ligand Precursor Aqueous Solutions at Room Temperature. *CrystEngComm* **2013**, *15* (18), 3601.
(28) Tai, M. F.; Lai, C. W.; Hamid, S. B. A.; Suppiah, D. D.; Lau, K. S.; Yehya, W. A.; Julkapli, N. M.; Lee, W. H.; Lim, Y. S. Facile Synthesis of Magnetite Iron Oxide Nanoparticles via Precipitation Method at Different Reaction Temperatures. *Mater. Res. Innovations* **2014**, *18* (sup6), S6-470−S6-473.
(29) Mos, Y. M.; Zorzano, K. B.; Buisman, C. J. N.; Weijma, J. Magnetite Synthesis from Ferrous Iron Solution at pH 6.8 in a Continuous Stirred Tank Reactor. *Water Sci. Technol.* **2018**, *77* (7), 1870−1878.
(30) Lu, Q.; Zhang, Y.; Hu, H.; Wang, W.; Huang, Z.; Chen, D.; Yang, M.; Liang, J. In Situ Synthesis of a Stable Fe_3O_4@Cellulose Nanocomposite for Efficient Catalytic Degradation of Methylene Blue. *Nanomaterials* **2019**, *9* (2), 275.
(31) Cao, S.-L.; Xu, H.; Lai, L.-H.; Gu, W.-M.; Xu, P.; Xiong, J.; Yin, H.; Li, X.-H.; Ma, Y.-Z.; Zhou, J.; Zong, M.-H.; Lou, W.-Y. Magnetic ZIF-8/Cellulose/Fe_3O_4 Nanocomposite: Preparation, Characterization, and Enzyme Immobilization. *Bioresour. Bioprocess.* **2017**, *4* (1), 56.
(32) Zhou, J.; Li, R.; Liu, S.; Li, Q.; Zhang, L.; Zhang, L.; Guan, J. Structure and Magnetic Properties of Regenerated Cellulose/Fe_3O_4 Nanocomposite Films. *J. Appl. Polym. Sci.* **2009**, *111* (5), 2477−2484.
(33) Min, X.; Yang, W.; Hui, Y.-F.; Gao, C.-Y.; Dang, S.; Sun, Z.-M. Fe_3O_4@ZIF-8: A Magnetic Nanocomposite for Highly Efficient UO_2^{2+} Adsorption and Selective UO_2^{2+}/Ln^{3+} Separation. *Chem. Commun.* **2017**, *53* (30), 4199−4202.
(34) Zhang, T.; Zhang, X.; Yan, X.; Kong, L.; Zhang, G.; Liu, H.; Qiu, J.; Yeung, K. L. Synthesis of Fe_3O_4@ZIF-8 Magnetic Core−Shell Microspheres and Their Potential Application in a Capillary Microreactor. *Chem. Eng. J.* **2013**, *228*, 398−404.
(35) Azizi, A. Green Synthesis of Fe_3O_4 Nanoparticles and Its Application in Preparation of Fe_3O_4/Cellulose Magnetic Nanocomposite: A Suitable Proposal for Drug Delivery Systems. *J. Inorg. Organomet. Polym. Mater.* **2020**, *30* (9), 3552−3561.
(36) Dong, L.; Zhang, C.; Gu, J.; Sun, Y.; Bai, Y.; Chen, M.; Xu, Y. Tuning the Size and Morphology of Zeolitic Imidazolate Framework-8 in a Membrane Dispersion Reactor. *New J. Chem.* **2015**, *39* (8), 5890−5894.
(37) Rehman, G. U.; Tahir, M.; Goh, P. S.; Ismail, A. F.; Hafeez, A.; Khan, I. U. Enhancing the Photodegradation of Phenol Using Fe_3O_4/SiO_2 Binary Nanocomposite Mediated by Silane Agent. *J. Phys. Chem. Solids* **2021**, *153*, 110022.
(38) Shi, H.; Li, W.; Zhong, L.; Xu, C. Methylene Blue Adsorption from Aqueous Solution by Magnetic Cellulose/Graphene Oxide Composite: Equilibrium, Kinetics, and Thermodynamics. *Ind. Eng. Chem. Res.* **2014**, *53* (3), 1108−1118.
(39) Yu, Z.; Qian, L.; Zhong, T.; Ran, Q.; Huang, J.; Hou, Y.; Li, F.; Li, M.; Sun, Q.; Zhang, H. Enhanced Visible Light Photocatalytic Activity of CdS through Controllable Self-Assembly Compositing with ZIF-67. *Mol. Catal.* **2020**, *485*, 110797.
(40) Chou, X.; Ye, J.; Cui, M.; Li, Y.; He, Y.; Liu, X.; Wang, H. Construction of 2D/2D Heterogeneous of ZIF-8/SnS_2 Composite as a Transfer of Band-Band System for Efficient Visible Photocatalytic Activity. *ChemistrySelect* **2019**, *4* (38), 11227−11234.
(41) Bahmani, M.; Dashtian, K.; Mowla, D.; Esmaeilzadeh, F.; Ghaedi, M. UiO-66(Ti)-Fe_3O_4-WO_3 Photocatalyst for Efficient Ammonia Degradation from Wastewater into Continuous Flow-Loop Thin Film Slurry Flat-Plate Photoreactor. *J. Hazard. Mater.* **2020**, *393*, 122360.
(42) Chen, W.-Q.; Li, L.-Y.; Li, L.; Qiu, W.-H.; Tang, L.; Xu, L.; Xu, K.-J.; Wu, M.-H. MoS_2/ZIF-8 Hybrid Materials for Environmental Catalysis: Solar-Driven Antibiotic-Degradation Engineering. *Engineering* **2019**, *5* (4), 755−767.
(43) Jin, X.; Ye, L.; Wang, H.; Su, Y.; Xie, H.; Zhong, Z.; Zhang, H. Bismuth-Rich Strategy Induced Photocatalytic Molecular Oxygen Activation Properties of Bismuth Oxyhalogen: The Case of $Bi_{24}O_{31}Cl_{10}$. *Appl. Catal., B* **2015**, *165*, 668−675.
(44) Tang, C.; Shen, X.; Wu, X.; Zhong, Y.; Hu, J.; Lu, M.; Wu, Z.; Zhang, Y.; Yu, W. W.; Bai, X. Optimizing the Performance of Perovskite Nanocrystal LEDs Utilizing Cobalt Doping on a ZnO Electron Transport Layer. *J. Phys. Chem. Lett.* **2021**, *12* (41), 10112−10119.
(45) Li, S.; Cai, M.; Liu, Y.; Wang, C.; Yan, R.; Chen, X. Constructing $Cd_{0.5}Zn_{0.5}S$/Bi_2WO_6 S-Scheme Heterojunction for Boosted Photocatalytic Antibiotic Oxidation and Cr(VI) Reduction. *Adv. Powder Mater.* **2023**, *2* (1), 100073.
(46) Zhang, H.; Gao, Y.; Meng, S.; Wang, Z.; Wang, P.; Wang, Z.; Qiu, C.; Chen, S.; Weng, B.; Zheng, Y. Metal Sulfide S-Scheme Homojunction for Photocatalytic Selective Phenylcarbinol Oxidation. *Adv. Sci.* **2024**, *11* (17), 2400099.
(47) Schumacher, L.; Marschall, R. Recent Advances in Semiconductor Heterojunctions and Z-Schemes for Photocatalytic Hydrogen Generation. *Top. Curr. Chem.* **2022**, *380* (6), 53.
(48) Wei, X.; Wang, X.; Pu, Y.; Liu, A.; Chen, C.; Zou, W.; Zheng, Y.; Huang, J.; Zhang, Y.; Yang, Y.; Naushad, Mu.; Gao, B.; Dong, L. Facile Ball-Milling Synthesis of CeO_2/g-C_3N_4 Z-Scheme Heterojunction for Synergistic Adsorption and Photodegradation of Methylene Blue: Characteristics, Kinetics, Models, and Mechanisms. *Chem. Eng. J.* **2021**, *420*, 127719.

https://doi.org/10.1021/acsomega.4c06142
ACS Omega 2024, 9, 49239−49248